J Mater Sci (2011) 46:5568–5580
DOI 10.1007/s10853-011-5507-7

Influence of pH on the synthesis and characterization of CuO powder for thick film room-temperature NH_3 gas sensor

Iqbal Singh · R. K. Bedi

Received: 20 October 2010 / Accepted: 23 March 2011 / Published online: 7 April 2011

Abstract CuO films of 51 μm thickness have been fabricated from nanocrystalline powder, which has been synthesized by a sol–gel auto-combustion method at different pH values of the precursor solution. Studies reveal that the pH value of the precursor solution strongly affects the decomposition rate of the metal–citrate complex formed by precursors (cupric nitrate and citric acid). Structural characterization of the powder samples shows a considerable change in agglomeration behavior, crystallite size and strain with variation in pH value of the precursor solution. Studies show that high pH reaction conditions results in the production of highly porous CuO nanoparticles with lowest crystallite size of 27 nm. Thick films of the synthesized material show an extremely high response of 0.941 to few parts per million level of ammonia at room temperature as well as possesses good stability for a long period of time. The adsorption of ammonia on the sensor surface obeys Elovich equation and the reaction kinetics followed is of first order. The lowest potential barrier of 0.50 MΩ and highest rate constant of 0.0136 s^{-1} have been found for ammonia adsorption on the sensor surface in case of film fabricated from CuO powder synthesized at high pH value of precursor.

I. Singh (✉)
Department of Physics, Khalsa College, Amritsar 143005, Punjab, India
e-mail: iqbalsgh@yahoo.com

R. K. Bedi
Material Science Laboratory, Department of Physics, Guru Nanak Dev University, Amritsar 143005, Punjab, India
e-mail: rkbedi2008@gmail.com

Introduction

Metal oxide nanostructures have drawn considerable attention in recent years because of their improved catalytic, optical and gas sensor properties, etc. [1, 2]. Different morphological nanostructures have different electronic, optical, and magnetic properties. Consequently, a large number of studies have been devoted to study metal oxide nanocrystalline powder and films due to their versatile application in different areas [3, 4]. Among the most studied transition metal oxide, CuO is a black solid acting as a semiconductor with direct band gap of 1.36 eV, which makes it a promising material to be used in device applications such as catalytic [2], lithium ion batteries, gas sensing [3] and in solar cells [5], etc. Recent studies on CuO have proved a remarkable effect of crystallite size, and agglomeration on device performance. As a sensor, CuO is proved to be highly efficient for detecting reducing and oxidizing gases at parts per million levels.

Variety of synthesis techniques like thermal evaporation [6], sol–gel spin coating [7], chemical [8], electrodeposition [9], vacuum annealing [10], polymer precursor [11], spray pyrolysis [12, 13], vacuum evaporation [14] and hydrothermal [15], etc. have been widely used for the preparation of nanocrystalline CuO powder and films. However, despite the excellent progress that has been made in the preparation of variety of nanomaterials using aforementioned techniques, there are several drawbacks. These techniques required sophisticated instruments, highly controlled reaction parameters, comparatively long reaction times and poor yield, and moreover, the purity of final product. The chemical precipitation and sol–gel methods have drawn considerable attention in the synthesis of metal oxide nanoparticles due to their simple processing route and as no sophisticated instrument is required [16, 17].

Moreover, the sol–gel auto-combustion synthesis seems to be an interesting and powerful method for the synthesis of metal oxide nanoparticles and has attracted considerable attention due to production of single–phase ceramics at relatively low temperatures, better compositional homogeneity, huge porosity, and purity of the synthesized powder [18–20]. The auto-combustion technique involves an exothermic chemical reaction which takes place between a fuel (e.g., citric acid, urea, glycine or glycol, etc.) and an oxidizer (e.g., metal nitrates) [21]. The large quantity of gases generated during the combustion process rapidly cools the product leading to nucleation of crystallites without any substantial growth [22, 23]. The nature, quantity of the fuel, and pH of the starting solution are important factors in preventing selective precipitation, and phase separation during the evaporation of solvents. All these factors must be carefully optimized to get best single phase nanostructures to be used in different electrical and optical device applications [24–26].

The effect of the fuel to oxidant ratio on the powder characteristics has been reported earlier [27, 28]. Using the concept of propellant chemistry, the calculation of oxidation and reduction valances for stoichiometric metal nitrate and citric acid solution are described in detail by Huang [29]. In our case this ratio was found to be 1:0.55 and in our previous report shows that this ratio results the combustion process in uncontrolled manner, and product formed is highly agglomerated copper oxide powder [28]. One way of controlling the combustion reaction is to make it sluggish by using a fuel rich precursor. Hence MN:CA ratio 1:1 has been proved to be a suitable and important parameter affecting the CuO powder characteristics. However, only a few efforts have been made to investigate the effect of the pH in combustion route to study the properties of metal oxide nanoparticles. The gel combustion process has been extensively employed in the last few years for the synthesis of nanoparticles of a number of metal oxides, such as SnO_2, NiO, yttria-stabilized zirconia and ferrites. On the other hand, a limited number of studies have been dedicated to the study of the gel combustion route to synthesize both pure and doped copper oxide nanopowders.

In this communication, a solution-based combustion synthesis technique has been exploited to fabricate thick films from nanocrystalline CuO powder. The effect variation in pH of precursor solution on the structural, morphological and electrical properties of CuO powder is investigated. The fabricated thick films were subsequently tested for electrical and gas sensing properties. Based upon the result, the kinetics of films toward 50 ppm ammonia gas is explored.

Experimental section

Cupric Nitrate ($Cu(NO_3)_2{\cdot}3H_2O$) and citric acid monohydrate ($C_6H_8O_7{\cdot}H_2O$) were used as starting materials. To make 0.5 M aqueous solution of cupric nitrate was prepared by dissolving 6.04 g of salt in 100 mL of deionized water. A calculated quantity of citric acid was added keeping molar ratios of metal nitrate to citric acid (MN:CA) 1:1. Liquid ammonia was then added to adjust the final pH of the solution to 2, 7, and 10. The pH of the solution was measured by microprocessor-based (Naina make NIG 334) pH meter. The solution was continually stirred using a magnetic stirrer for 4 h and followed by thermal dehydration in an oven at temperature of 80 ± 5 °C. The viscous liquid so obtained was heated on a preheated hot plate. The material undergoes foaming and large quantities of gases were evolved. The spontaneous ignition occurred, causing enormous swelling of the gel and producing a blackish, foamy, voluminous decomposed mass. The detailed combustion mechanism has been reported earlier [28].

Thermal treatment

The decomposed gel samples so obtained for pH 2, 7, and 10 were subjected to post thermal treatment at 400 °C for 4 h in muffle furnace (Macro Scientific) with heating rate of 10 °C/min. The thermal analysis shows that no significant weight change has been observed beyond 400 °C in samples prepared with different pH value. This shows the thermal stabilization of the samples [28]. Because of these observations, the best temperature of calcination is chosen to be 400 °C. The calcined samples were allowed to cool in muffle furnace till the room temperature has been attained. The calcination results in the production of fine nanocrystalline CuO powder without any impurity. The calcined powder samples were named as P2, P7, and P10 according to the pH value 2, 7, and 10, respectively, of the precursor solution.

Thick film fabrication

A known quantity of calcined CuO powder was thoroughly ground in an agate pestle mortor to ensure sufficient uniform fine particles. The fine powder so obtained was used in making thixotropic paste by mixing CuO powder with an organic solvent diethnolamine, which acts as binder. The ratio of inorganic to organic part was kept equal to 75:25 in all cases. The fluidity of the paste depends upon the extent of the organic part, which goes in its formulation. This particular ratio for the paste formation was found to be

thixotropic in nature and gives good adhesion to substrate. A uniform layer of the thixotropic paste was then deposited on ultrasonically cleaned glass slides. The films were then subjected to spun on a spin coater (Macmillan) under 4,000 rpm for 5 min to allow the uniform distribution of the paste. The films were further dried at 400 °C in the muffle furnace for 1 h to burn out the organic binder. The thickness of the films were monitored using depth profiler (Dektek 3030 XT) and was found to be around 51 ± 0.5 μm. The reproducibility in the thickness of the films was possible by maintaining proper rheology and thixotropy of the paste.

Thermal analysis

The thermal analysis of the dried gel samples (approximately equal in weight) was carried out using Perkin Elmer (Pyris diamond) thermal analyzer. Air was used as a purged gas in the analysis. The scan rate and air flow rate of 10 °C/min and 50 mL/min, respectively, were taken with alumina powder as a reference material.

X-Ray diffraction analysis

The phase identification of the decomposed gel and the calcined powder samples was performed by X-ray diffraction (XRD) on a X'Pert Panlytical diffractometer using Cu Kα radiation ($\lambda = 1.5405$ Å, 30 mA, 40 kV) in 2θ range from 30° to 80°.

FESEM and TEM analysis

The surface topography of CuO powder sample was studied by scanning electron micrographs taken using JEOL JSM-6700F with a beam voltage of 30 kV. TEM images were taken using transmission electron microscope system (HRTEM, model FEI Technai 30) operated at 300 kV.

Electrical characterization

The electrical conductivity measurements on the films were carried out using two probe technique by heating it on a specially designed heater. The temperature of the film samples were measured using a K-type (chromel–alumel) thermocouple obtained from Omega Engineering Inc. (USA).

Gas adsorption kinetics

The films were tested for their sensitivity toward ammonia gas at room temperature. The sensitivity has been calculated by measuring the corresponding change in film resistance in presence of air and NH_3 gas atmosphere at room temperature (300 K) in measuring cell of volume 500 cm^3, using Keithley 6517A electrometer having in built source of constant voltage power supply.

Results and discussion

Thermal analysis

Figure 1a–c shows the TGA/DTA plots of the dried metal–citrate complex obtained at different pH values. The thermal decomposition of the dried precursor collected prior to pyrophoric decomposition can be clearly seen in the TGA/DTA plots. The mechanism of combustion reaction can be formulated in terms of equation as follows:

$$9Cu(NO_3)_2 + 5C_6H_8O_7 = 9CuO + 30\ CO_2 + 9N_2 + 20H_2O \quad (1)$$

A gradual weight loss of 10–15% in TGA plots occurs in the temperature range 100–200 °C, which is due to the removal of residual water in the dried gel. The exothermic behavior of auto-ignition can be clearly seen in the temperature range 195–240 °C, for which concurrent weight loss of about 50–95% occurred in all the dried gel samples. The maximum weight loss (TGA plot) occurs in a very narrow temperature range corresponds to auto-ignition of the dried gel. The weight loss of 69.27% has been observed in case of dried gel obtained with pH 7. Comparatively lesser weight loss for the dried gel precursor having pH value 2 and 10 has been found approximately 48.95 and 47.38%, respectively.

DTA plots shows that the combustion rate was influenced significantly with the change in pH value of the precursor solution. The onset of decomposition and the full width at half maximum (FWHM) of main exothermic peak are also found to be varying with pH. With increase in pH value of the precursor solution from 2 to 10, the rate of combustion for the corresponding dried gel increases, as evident from the decrease in FWHM of exothermic peaks. The corresponding weight loss has been observed to be decreased from 95 to 77.65%. For pH 2, the exothermic peak centered around 240 °C, with FWHM of 14.70 °C has been observed. For sample obtained with pH value 7 and 10, the peak shifts to 206 and 228 °C, having FWHM of 9.46 and 8.63 °C, respectively. The intensity of the peak increases drastically, whereas the FWHM decreases with increase in pH of the precursor solution. This result is in accordance with the observation reported by Vajargah [26]. Authors have suggested that rise in pH would lead to an increase in NO_3^- ion content in the reaction mixture, and hence increases the decomposition rate, as the nitrate ions

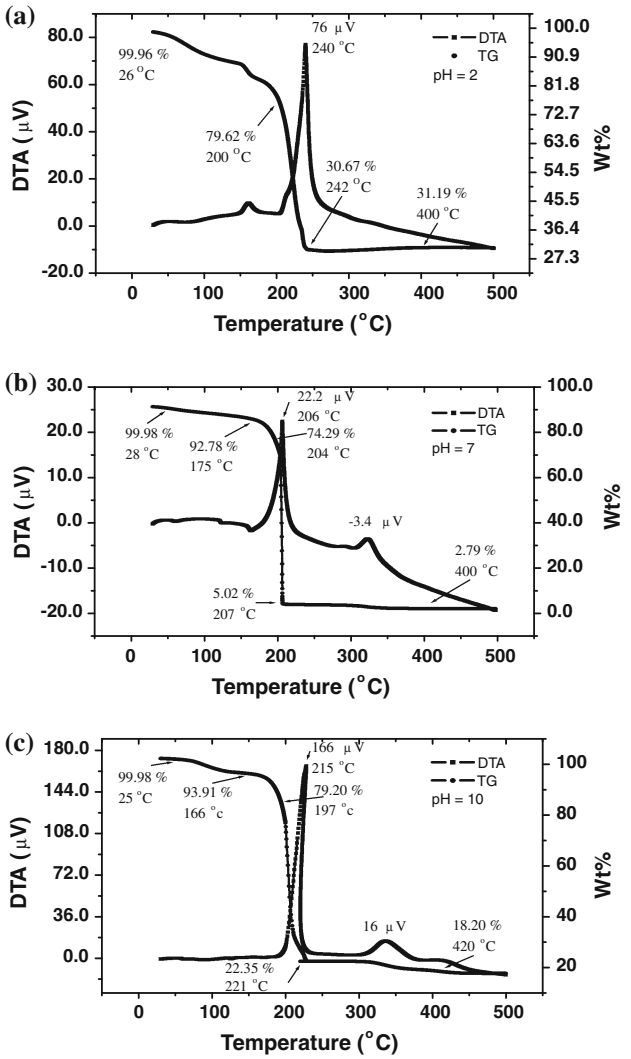

Fig. 1 TG–DTA curves of dried gel samples collected prior to decomposition at pH **a** 2, **b** 7, and **c** 10

provide an in situ oxidizing environment for the decomposition of organic compound. It is found that main exothermic peak appeared in DTA plot is weakened and broadened with the decrease in pH from 10 to 2. This results in reduced exothermicity and prolonged time of auto-ignition reaction.

The second exothermic peak of weaker intensity appeared in DTA plot for pH 7 and 10 samples at temperature around 323 and 338 °C, respectively, show the burning of unreactive organic matter induced by citric acid and nearly 1–4% weight loss has been observed in the reaction and leaves the system as CO_x ($x = 1, 2$) gases. Huang [29] have also reported the emission of similar gases in the temperature range 220–420 °C for the synthesis of $BaFe_{12}O_{19}$. Investigations reveal that the increase in pH value in the reaction mixture results an enhancement in the exothermicity of the reaction, and thus play a pivotal role as a catalyst.

The TGA plot shows that no significant weight change has been observed beyond 400 °C in samples prepared with different pH value, which ensures that no carbon is present above this temperature and all the oxidation and reduction reactions and phase transformation take place below this temperature. This shows the thermal stabilization of the samples [28]. Because of these observations, the best temperature of calcination is chosen to be 400 °C.

X-ray diffraction analysis

X-ray diffractogram of the decomposed gel samples obtained at different pH value are illustrated in Fig. 2. The diffractogram shows the powder obtained is polycrystalline in nature and the peak corresponding to Cu_2O and CuO phases have been appeared in decomposed gel powders. Diffractogram shows an intense diffraction peaks corresponding to (002) and (111) atomic planes of CuO phase located at 2θ value 35.5 and 38.7°, respectively, in all decomposed gel powders. A peak having lower intensity of (111) atomic plane of Cu_2O at 2θ value of 36.4° of comparatively smaller intensity has been appeared in diffractogram. In addition, the reflections from (111) and (200) atomic planes of Cu at 2θ value 43.30 and 50.40°, respectively, can also seen in the XRD pattern. The appearance of Cu peaks in the diffractogram might be due to insufficient time as the combustion process ends up in few minutes. Thus, complete oxidation of Cu does not takes place. The combustion process CuO was found to be the major content in decomposed gel powders. It can be observed that the intensity of Cu_2O peak goes on decreasing with increase in pH value. This might be due to increase in local temperature, which enhances the oxidation rate of Cu_2O to CuO phase. This observation is in accordance with thermal analysis, and with the observation reported by Peng [22] in the synthesis of alumina powder. The percentage composition of Cu_2O and CuO in the decomposed gel has been calculated with the help of intensity of prominent diffraction peaks corresponding to these phases by using the formula given below

$$\mathrm{CuO}\ (\%) = \frac{I_{\mathrm{CuO}}(200) + I_{\mathrm{CuO}}(111)}{I_{\mathrm{CuO}}(200) + I_{\mathrm{CuO}}(111) + I_{\mathrm{Cu_2O}}(110)} \times 100$$

$$\mathrm{Cu_2O}\ (\%) = \frac{I_{\mathrm{Cu_2O}}(110)}{I_{\mathrm{CuO}}(200) + I_{\mathrm{CuO}}(111) + I_{\mathrm{Cu_2O}}(110)} \times 100 \quad (2)$$

where $I_x(hkl)$ is the intensity of the corresponding to (hkl) plane of x phase in the material. The ratio of CuO:Cu_2O percentage composition in the decomposed gel sample obtained with pH 2 is calculated to be 67.89:32.11. This

ratio changes to 84.01:15.99 and 84.43:15.57 for decomposed gel obtained with pH 7 and 10, respectively. Thus, it has been observed that the content of Cu_2O has been decreased whereas CuO has been increased in the decomposed gel samples with increase in pH. This observation is in conformity with the thermal analysis that proves that increase in pH would provide an oxidizing environment to combustion process.

The crystallite size in decomposed gel samples was calculated for most prominent (002) diffraction peak of CuO phase by using the Scherrer's formula [30],

$$D = \frac{0.9\lambda}{\beta \cos\theta} \tag{3}$$

where $\lambda = 1.5405$ Å for Cu Kα radiations, β is the FWHM of the diffraction peaks in radians, and θ is the Bragg angle. The crystallite size has been found to be 27.82, 31.49, and 23.04 nm for decomposed gel obtained from pH 2, 7, and 10, respectively.

The XRD diffractograms of the decomposed gel powder calcined at 400 °C are shown in Fig. 3. The all prominent reflections on the pattern can be indexed for monoclinic CuO phase. The peak positions are in agreement to those reported by International Center for Diffraction Data (ICDD) card 41-254. The high intensity, prominent peaks of (002) and (111) atomic planes of CuO shows the grain growth, as this is most stable phase in the decomposed gel.

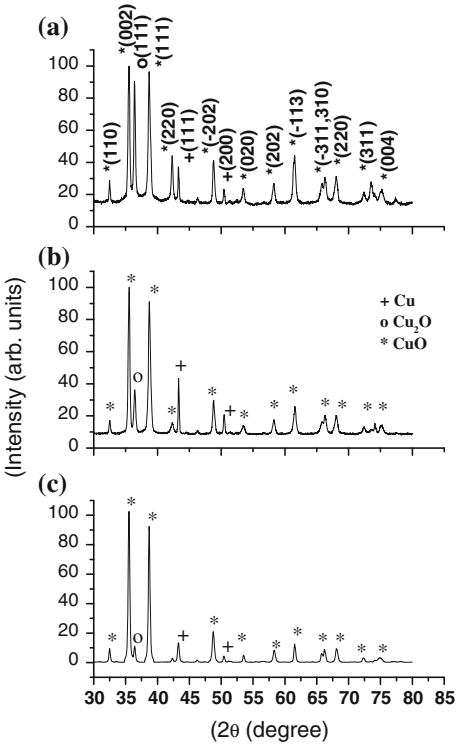

Fig. 2 XRD spectrum of the decomposed gel sample at pH value **a** 2, **b** 7, and **c** 10

In addition, the other low intensity peaks of (110), (−220), (020), (202), (−113), (−311), (310), (220), (311), and (004) atomic planes of CuO has been also noticed. Interestingly, no other peak corresponding to any of the source material, Cu and Cu_2O has been noticed. It is believed that [31] the presence of the Cu_2O phase in the decomposed gel acts like catalyst site for the formation of CuO. The conversion of the Cu_2O into CuO results from the diffusion of oxygen atoms and can be represented by the reaction

$$2Cu_2O + O_2 = 4CuO \tag{4}$$

Figure 4 shows the XRD diffractogram of the CuO thick film. It is interesting to note that all the characteristic peaks of CuO as described above have been appeared and no extra peak corresponding to the organic binder has been observed. This indicates that the binder has no influence on the crystallinity of CuO.

The crystallite size for P2, P7, and P10 samples has been found to be 29.36, 63.40, and 27.73 nm, respectively. This observation obtained from the XRD analysis is in conjunction with thermal analysis. The crystallite size has been found to be enhanced in P7 sample as compared to P2 and further a reduction in size has been found for P10 sample. The variation in the size might also be dependent upon how the combustion reaction takes place. As evident from the DTA analysis of P7 sample, the existence of a comparatively weak exothermic peak of 22 μV, suggesting lesser quantity of gas evolution in the reaction as compared to in P2 and P10 samples. Hence the decomposed gel so obtained for P7 sample is highly agglomerated and significant reduction in pore structure leads to merging of grains at a much faster rate in the applied post thermal treatment under identical condition in comparison to P2 and P10 samples. For P10 sample comparatively strong exothermic peak generates more porous network which hinder the merging of

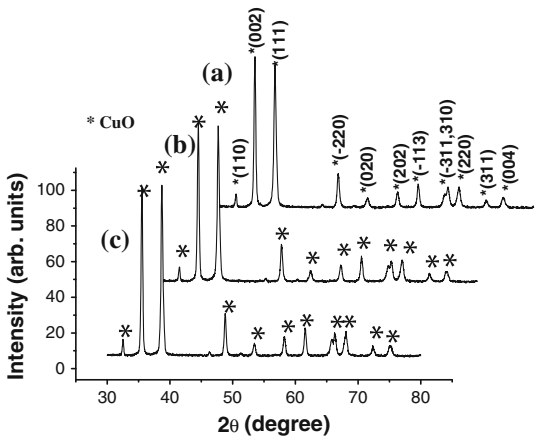

Fig. 3 XRD spectrum of the decomposed gels calcined at 400 °C obtained at pH 2, 7, and 10, respectively. Figure shows the diffractogram **a** P2, **b** P7, and **c** P10 samples

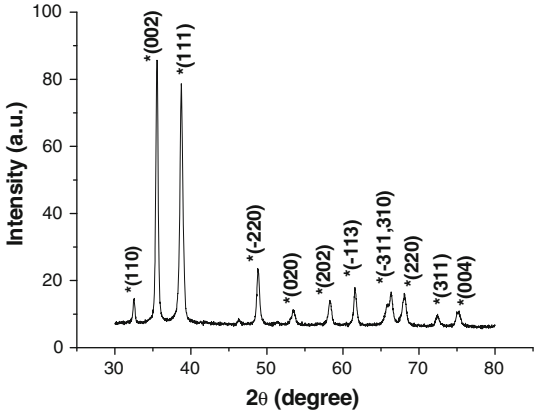

Fig. 4 XRD spectrum of the CuO thick film of P7 sample deposited onto the glass substrate. No peak corresponding to the organic binder has been appeared in the pattern

grains in post thermal treatment. Thus increase in pH of the precursor solution suggesting a decrease in crystallite size. Xu [32] have been observed a similar effect of pH on the characteristics of $BaFe_{12}O_{19}$ powder prepared by similar technique. They have reported that increase in pH resulted in the decrease in crystallite size. The FWHM can be interpreted in terms of lattice strain by the following Hall–Wlliamson equation [33] expressed as:

$$\frac{\beta\cos\theta}{\lambda} = \frac{1}{D} + \frac{\varepsilon\sin\theta}{\lambda} \tag{5}$$

where β is the FWHM of the peak, θ the Bragg angle, λ the wavelength, D is the effective crystallite size, and ε is the effective strain. The ε values were calculated from the least square fit to $\frac{\beta\cos\theta}{\lambda}$ vs. $\frac{\sin\theta}{\lambda}$ plots for the prominent peaks having comparatively higher intensity for the decomposed gel and calcined CuO samples as shown in Fig. 5. The average crystallite size was calculated from the intercept of plots and values has been found to be about 20, 38.61, and 12.82 nm for P2, P7, and P10 samples, respectively. The slight discrepancy in crystallite size, calculated using two ways might be because of, the Scherrer's formula considers most prominent peak, and Hall equation gives the average from all the significant peaks located at different 2θ value. The plot of Hall equation for the decomposed gel obtained from precursor having pH 2 and 7 showing positive slope, thus indicates the presence of tensile strain in lattice. Further, P2 and P7 samples also similar type of strain, and the magnitude strain decreases with calcination. Interestingly, in case of the decomposed gel and corresponding P10 sample, negative slope attributed to the presence of compressive strain. The decrement in strain with calcination is conformity with the increase in crystallite size. The strain is manifestation of dislocation network, and the decrease of strain indicates a decrease in concentration of lattice imperfections. The crystallite size and improvement

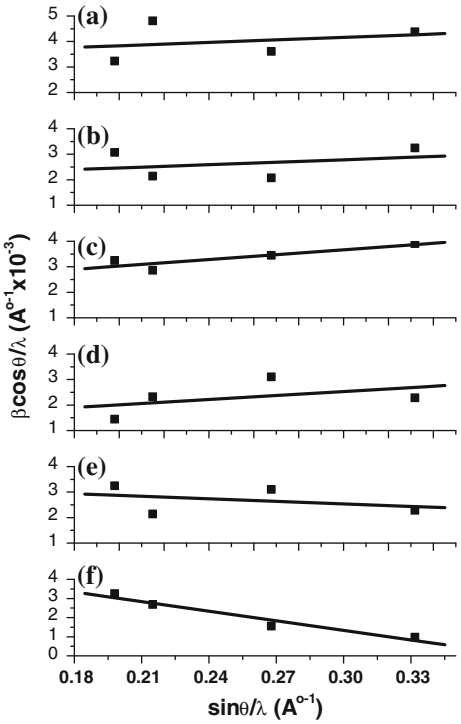

Fig. 5 Plot of Hall equation for the decomposed gels and corresponding sample calcined at 400 °C at pH 2 (**a**, **b**); 7 (**c**, **d**); and 10 (**e**, **f**), respectively

in crystallinity with calcination also support the observation.

To study the effect of the strain on the CuO powder the lattice parameters ($a \neq b \neq c$, $\alpha = \gamma = 90° \neq \beta$ for monoclinic structure) and the volume of unit cell have been calculated using the relations

$$\frac{1}{d^2} = \frac{1}{\sin^2\beta}\left(\frac{h^2}{a^2} + \frac{k^2\sin^2\beta}{b^2} + \frac{l^2}{c^2} - \frac{2hl\cos\beta}{ac}\right) \tag{6}$$

$$V = abc\sin\beta \tag{7}$$

where d is the interplanar spacing, h, k, l are Miller indices of the crystal planes, a, b, c, β are the lattice parameters, and V is the volume of the unit cell. The values of the lattice parameters with estimated error are recorded in Table 1 and found to be in good agreement with those reported by ICDD card. The lattice parameters show a decreasing trend in magnitude with increase in pH. The calculated value of lattice parameters a, b, and c reduces to 4.673 from 4.691, 3.423 from 3.428, and 5.109 from 5.112 Å, respectively, with increase in pH from 2 to 10. The value of β (degree) decreases to 99.098 from 99.251. A comparison of the calculated lattice parameters with one those reported for bulk CuO in literature, have been found to be lower in magnitude. This implies that lattice structure in CuO sample synthesized by auto-combustion method have more defects. The amount of defects has been found

to be enhanced with increase in pH and might also be responsible in improving the gas sensing properties of the material. The variation in pH of the precursor solution causes the unit cell volume is found to decrease with increase in pH value. Results reported earlier by Ramgir [34] confirms the observation that, increase in cell volume gives rise to tensile strain while reduction in the compressive strain. This suggests that the size-dependent strains in the particles are governed by the pH value of the precursors.

FESEM and TEM analysis

The FESEM images for P2, P7, and P10 samples are shown in Fig. 6. The porous feature of the agglomerates may be attributed to the liberation of large quantity of gas in the reaction. The particles appear to bound together into agglomerates of different shapes and sizes. The morphology of the decomposed gel calcined at 400 °C changes to aggregates of nanoparticles (Fig. 6a, b). The particle size in P10 sample lie in the range 20–30 nm, while in P7 sample, it is comparatively large around 125 nm.

TEM images for P2, P7, and P10 samples are shown in Fig. 7. The TEM images of samples also show the porous and loosely agglomerated CuO particles. The TEM images show that particle possesses no definite shape in P2 and P7 samples. P10 samples tend to possess nearly spherical morphology. The morphology the P7 sample shows bigger aggregates, consisting primary particles with size distribution of 20–80 nm (centered at 50 nm). For the P10 sample TEM images (Fig. 7b) exhibited a sharp particle size distribution with an average particle diameter of 22–25 nm. This value is very close to that of crystallite size (27.73 nm) calculated from XRD pattern for the same sample, implying the obtained CuO powder have good crystallinity, and low agglomeration. The inconsistency in crystallite size measurement in from XRD and TEM is not known exactly. The possible reason in case of P7 sample is the appearance of hard agglomerates which were difficult to resolve separately in TEM measurements.

The variation in the shape and size of the CuO nanoparticles is in fact the consequence of the reaction conditions during the powder preparation. The particle size and the agglomeration in the material depend mainly on the way the combustion propagates and the amount of disintegration occurs. The higher reaction temperature associated with sample having pH 7 appears to calcine the formed particle and consequently, the particles grow as the reaction propagates even during the post thermal treatment applied to remove the organics. Similar results have been discussed during the synthesis of $LiMn_2O_4$ and Ni-YSZ cermet electrodes using combustion synthesis technique by Kovacheva [35] and Marjan [36]. The decrease in agglomeration as observed in FESEM images of P10 sample may be assigned to the large quantity of the gas evolved with an increase in pH.

Mechanism of the reaction

The sol–gel route is a chain process where the quality of the final product depends upon the intermediate steps. The most important and significant steps towards the formation of gel are the pre-hydrolysis, hydrolysis and polycondensation. The rate of all these determine the gel structure and

Table 1 Shows the values of the lattice parameters, strain and crystallite size calculated from X-ray diffraction plot, crystallite size from TEM measurement, activation energy, response, initial adsorption rate, potential barrier, and '*k*' sensor response rate constant for the samples calcined at 400 °C with different pH value

Property	pH 2	pH 7	pH 10
a (Å)	4.691 (0.0025)	4.682 (0.0006)	4.673 (0.0012)
b (Å)	3.428 (0.0008)	3.424 (0.0020)	3.423 (0.0023)
c (Å)	5.112 (0.0046)	5.114 (0.0042)	5.109 (0.0052)
β (Degree)	99.251 (0.0001)	99.111 (0.0015)	99.098 (0.0016)
V cell volume (Å^3)	81.148 (0.0869)	80.949 (0.0822)	80.693 (0.1005)
Strain (ε) (tensile)	0.0018 (tensile)	0.0010 (tensile)	−0.0117 (compressive)
D crystallite size (nm) XRD (Scherrer's formula)	29.36	63.40	27.73
Crystallite size (nm) TEM	30	50	25
E_a activation energy (eV)	0.471	0.222	0.507
S Response	−0.673	−0.820	−0.941
a' (initial adsorption rate) × 10^{-8}	0.3	0.2	9.0
α (MΩ)	0.93	1.00	0.50
$\ln(C_e - C_t)$ vs. t (R^2)	$-0.0078X - 11.073$ (0.9018)	$-0.0093X - 12.513$ (0.9669)	$-0.0136X - 11.99$ (0.9397)
k (sensor response rate constant) s^{-1}	0.0078	0.0093	0.0136

[a] Minus sign with the response means that the sensor's resistance decreases during the gas hit

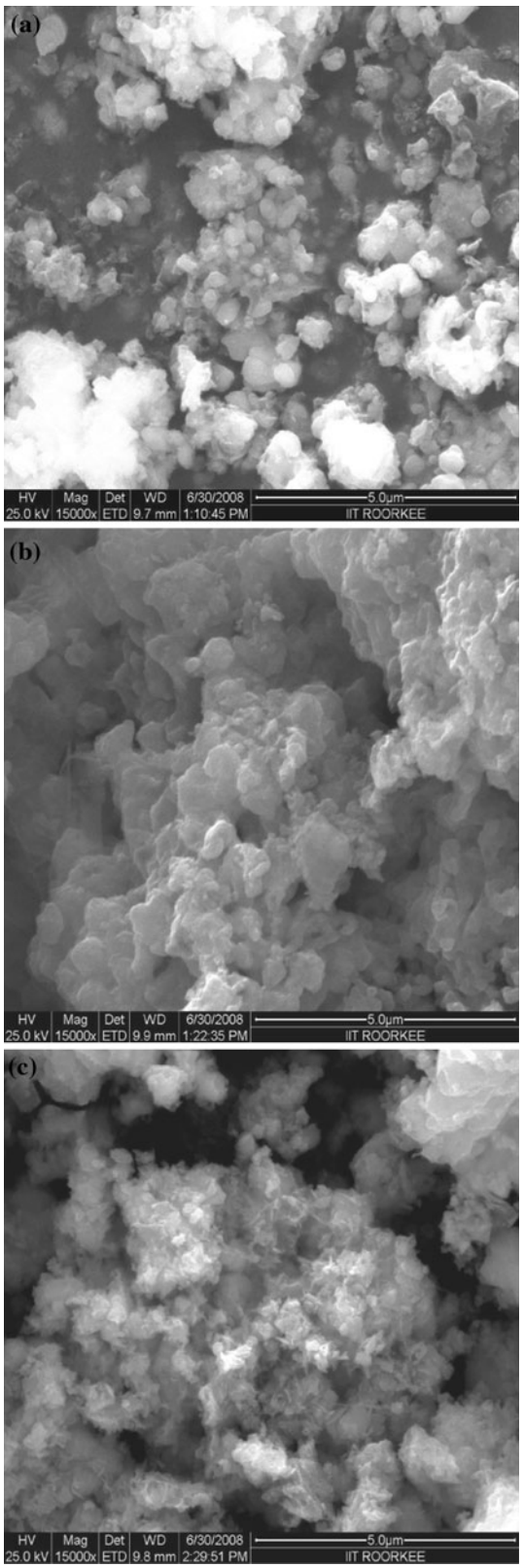

Fig. 6 FESEM images of CuO embedded in **a** P2, **b** P7, and **c** P10 samples, respectively, on 5.0 μm scale

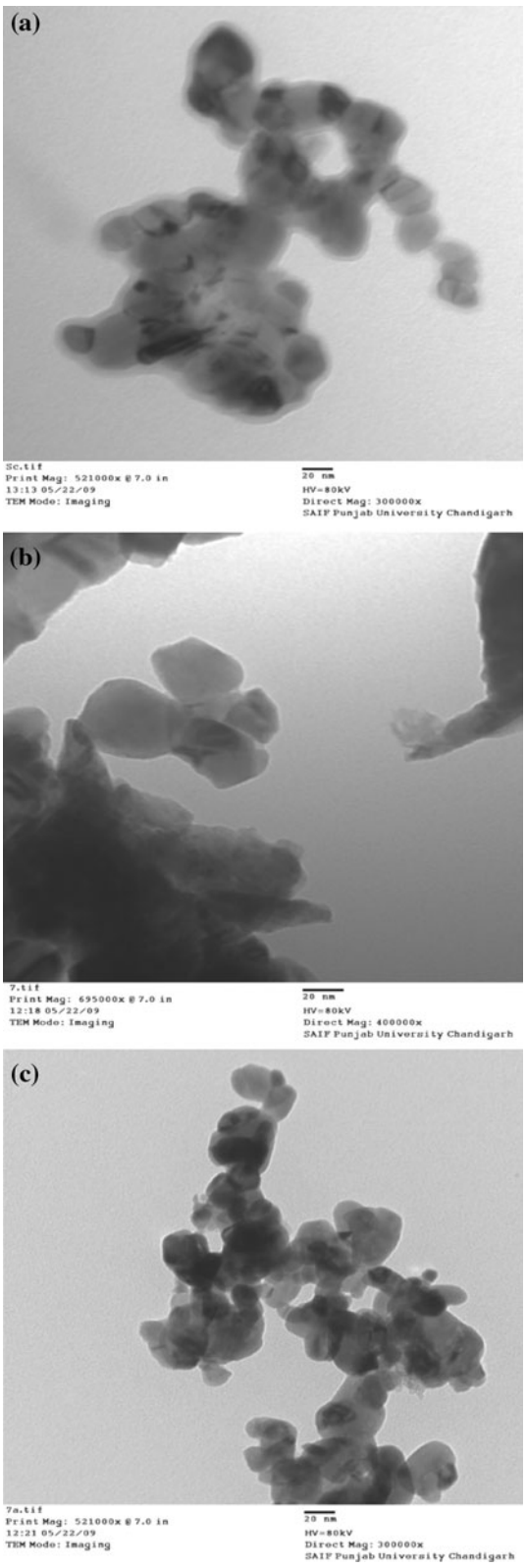

Fig. 7 TEM images of CuO embedded in **a** P2, **b** P7, and **c** P10 samples, respectively, on 20 nm scale

its properties. The reaction, taking place during ionization of citric acid at different pH values [37], is as follows:

$$H_3Cit = H_2Cit^- + H^+ \leftrightarrow \ pH < 3 \quad (8)$$

$$H_2Cit^- = HCit^{2-} + 2H^+ \leftrightarrow 3 < pH < 6.5 \quad (9)$$

$$HCit^{2-} = Cit^{3-} + 3H^+ \leftrightarrow \ pH > 6.5 \quad (10)$$

These reactions show that when the pH is acidic, citric ionization is very low, so the role of complexation by the citric acid becomes weak. Also, when the pH is increased to 7 (neutral), citric anions are as Cit^{3-}, so the role of complexation by the citric acid is the highest in slightly alkaline medium because the number of bonding between citrate anions and metallic cations has been increased. Therefore, a more homogenized gel will be prepared. The higher amount of H^+ ions in low pH conditions results in the formation of hydronium ions (H_3O^+), which inhibits the hydrolysis, and condensation process. On the other hand, the hydrolysis, and polycondensation rates towards the formation of gel were faster in the case for the precursor sol having higher pH, thus results in highly branched metal–oxygen polymeric network. The polymeric network obtained at high pH when burnt in the auto-combustion reaction results in the formation of highly porous CuO powder. From the thermal analysis, and XRD results, it also seems that the effect of ammonia was not only to adjust the pH value but also to form NH_4NO_3, which can liberate gases NO_x and O_2 in the combustion process. The large amount of gases liberation in higher pH condition is conferred from the sharpness of the exothermic peak. Peng [22] has also reported similar observation on the effect of acidity on the synthesis of alumina powder.

Electrical characterization

The electrical resistance of the films was measured as function of temperature (300–473 K). The P7 film resistance has been found to be 1.71 MΩ at room temperature, whereas it is 3.37 and 3.41 MΩ for P2 and P10 films, respectively. The decrease in film resistance with temperature is quite likely as large number of oxygen molecules are chemisorbed at the grain boundary and on the surface of the film. The principal chemisorption species in CuO is O_2^{-1} at room temperature [38]. With the rise in temperature, the rate of chemisorption of O_2^{-1} increases on the sample surface, which results in the decrement of surface resistance of films. The dependence of conductivity on temperature can be represented by the Arrhenius equation [39]

$$\sigma = \sigma_0 \exp\left(-\frac{\Delta E_a}{kT}\right) \quad (11)$$

where ΔE_a is the activation energy that corresponds to the energy difference between valence band and conduction band, σ_0 is a temperature independent factor, and k is the Boltzman's constant, and T absolute temperature. Figure 8 depicts the $\ln\sigma$ vs. $1000/T$ plots for films along with the correlation coefficient (R^2). The linear nature of the plots is indicated by the high R^2 value, implies that the thermionic emission plays a major role in the carrier transport [40]. The activation energies (recorded in the Table 1) of the samples have been obtained from the slope of plots. The variation in activation energy with pH can be understood from the decrease in crystallite size, as confirmed by XRD, and TEM analysis. The pre-exponential factor, which often reflects the charge carrier concentration is maximum 0.101 for P7 sample and decreases to 0.021 and 0.002 for P2 and P10 sample, respectively. Thus, the electrical conductivity decreases in P2 and P10 samples as indicted from the enhancement in the activation energy. The decrease in crystallite size enhances the scattering of carriers at grain boundaries, thus results a decrease in the mobility as suggested by Bouderbala [41]. The porous nature of the CuO nanocrystallites might also be responsible for the increases in resistance, hence activation energy. Similar reports have also been there literature, as the effect of porosity on the electrical conductivity in case of Fe-based samples studied by Perez-Ramos [42].

Gas adsorption kinetics

The response of CuO thick films to 50 ppm ammonia gas at room temperature are shown in the Fig. 9. A decrease in

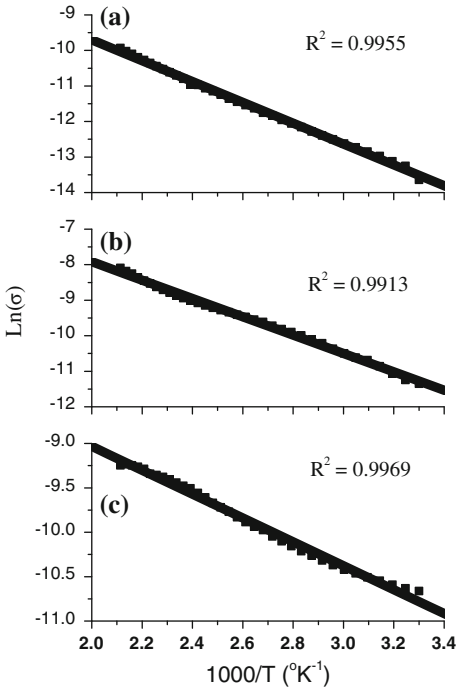

Fig. 8 Ln(σ) vs. $1000/T$ plot for the CuO films of **a** P2, **b** P7, and **c** P10 samples

surface resistance of the film has been observed with the introduction of ammonia in the testing cell. This may be assigned to the redox reaction of ammonia with the adsorbed oxygen species O_2^-. Evidently, CuO thick films have been found to show good sensing performance, with high sensitivity. Gas response (S) for a sensor is calculated using the formula given below and is defined as the ratio of change in the resistance on exposure to gas to the resistance in air.

$$S = \frac{|R_g - R_a|}{R_a} \tag{12}$$

where R_g and R_a are CuO thick film resistance, measured in ammonia and air atmosphere, respectively. The time taken for the sensor to attain 90% of the maximum change in resistance on exposure to the target gas is the response time. The time taken by the sensor to get back 90% of the original resistance is the recovery time. The response of the sensor has been found to be for 0.820 and 0.941 for P7, and P10 tested samples. The higher response in case of P10 sensor may be attributed to the small crystallite size and huge porosity in the material as suggested by Jimenez [43]. The recovery for P2 and P7 films has been about 53 and 58%, respectively, in 500 s. Interestingly, the increase in P10 films, it reaches to 92% in the same time. The detailed sensing mechanism of CuO-based ammonia sensors has been discussed in our previous report [44].

The adsorption of gas on the surface of a solid without desorption of products, leads to decrease in reaction rate. The increase in surface coverage reduces the active sites for the redox reaction to take place hence rate of the reaction decreases [45]. One of the most useful models for describing such activated chemical adsorption is Elovich equation [46], which is given by:

$$\frac{dq}{dt} = a' e^{-\alpha q} \tag{13}$$

where q is the quantity of gas adsorbed during time t, α, and a' are the constants during any one experiment. The kinetic law of chemisorption was established in depth by Zedowitsch [47]. To simplify Elovich's equation, Chien and Clayton [48] assumed that $a'\alpha t \gg 1$ and applying the boundary conditions of $q = 0$ at $t = 0$ and $q = q$ at $t = t$, then following equation

$$q = \frac{1}{\alpha}\ln(t + t_0) - \frac{1}{\alpha}\ln(t_0) \tag{14}$$

reduces to

$$q = \frac{1}{\alpha}\ln(a'\alpha) + \frac{1}{\alpha}\ln(t) \tag{15}$$

Thus, the constants can be using slope and intercept from the plot of q against $\ln(t)$. In the Elovich equation,

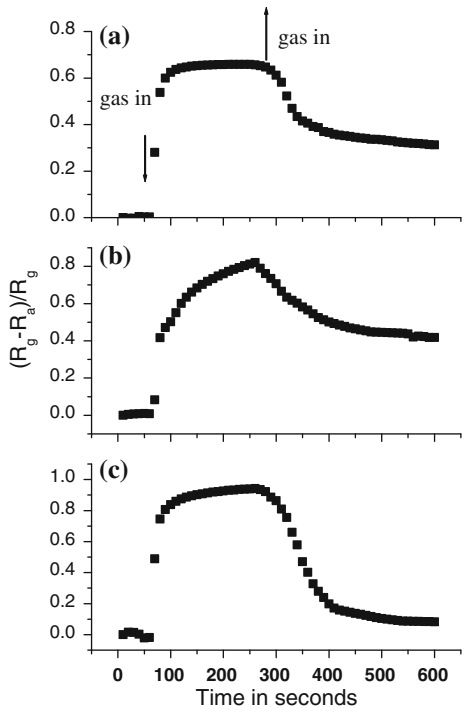

Fig. 9 Response for ammonia at room temperature of CuO films of **a** P2, **b** P7, and **c** P10 samples

constant a' is regarded as the initial adsorption rate, and it depends on the activation energy [49]. Constant α is related to a measure of the extent to which the surface has been screened by potential barrier for successive adsorption. Ammonia adsorption leads to a charge transfer between film and gas molecules. However, this process is limited by a potential barrier formed from the dipole layer created by the redistribution of charge between the NH_3 molecule and CuO film. The potential barrier increases with successive adsorption which induces surface heterogeneity. In present study, the change in conductance ΔC is proportional to the amount of the adsorbed NH_3 (q). The plot of ΔC vs. $\ln(t)$ is linear after a time of 100 to 110 s for thick films samples as evident in Fig. 10, thus indicating that the adsorption of ammonia on the surface of CuO films is in accordance with the Elovich equation. The values of the constants a' and α were obtained from the plot, and corresponding values are recorded in the Table 1. The initial adsorption rate has been found to be lowest for the P7 sample, whereas it was highest for films made from the P10 sample. The value of α, which represents the barrier for the successive adsorption is found to be larger for P2 (0.93 MΩ) and P7 (1 MΩ) samples, whereas it minimum of 0.50 MΩ for P10 sample.

The kinetics of the reaction between adsorbed ammonia and available oxygen species on the film surface has been determined from the plot of $\ln(C_e - C_t)$ vs. t and C_t vs. $\frac{C_t - C_0}{t}$ for the first and second-order reaction, respectively, using the method adopted by Tongpool [45] and

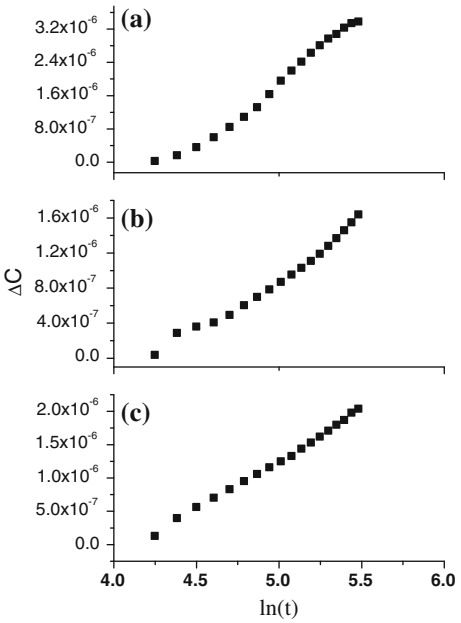

Fig. 10 Variation of change in conductance (ΔC) vs. ln(t) for CuO films of **a** P2, **b** P7, and **c** P10 samples

Kamalpreet [50]. The conformity between the experimental data and the model predicted values is expressed by correlation coefficient (R^2 values close or equal to 1). A relatively high R^2 value indicates that the model successfully describes the kinetics of the gas adsorption. The regression equations and R^2 values for the first order reaction are shown in Table 1. The highest R^2 value for the first order in all samples shows that the reaction between the ammonia and adsorbed oxygen species on the surface of CuO films is of first order. The non linear variation of C_t vs. $(C_t - C_0)/t$ as shown in the inset of Fig. 11, which shows the failure of second-order reaction mechanism. The sensor response rate constant k for the first-order reaction has been determined from the slope of the plot in Fig. 11 and is found to be 0.0078, 0.0093, and 0.0136 s^{-1} for P2, P7, and P10 samples, respectively. The rate constant for the P10 films has been found to be highest thus indicating the fastest reaction between ammonia and oxygen species in these cases. The poor recovery in case of P2 and P7 sensors in comparison to P10 makes it poor choice to be used it as an effective room temperature operating sensor.

Though the gas sensor based on CuO thick film shows comparatively better response toward NH_3 at room temperature as compared to the CuO sensor tested by Alexy [51]. The list of most commonly used thick film-based ammonia sensor is given in Table 2. It is interesting to reveal that the ammonia gas sensor based on CuO show much better response at room temperature in comparison to n-type materials like ZnO and SnO_2 at 100 °C [3]. Table 2 shows that the ammonia response of the room temperature operated sensor has been discussed for greater than

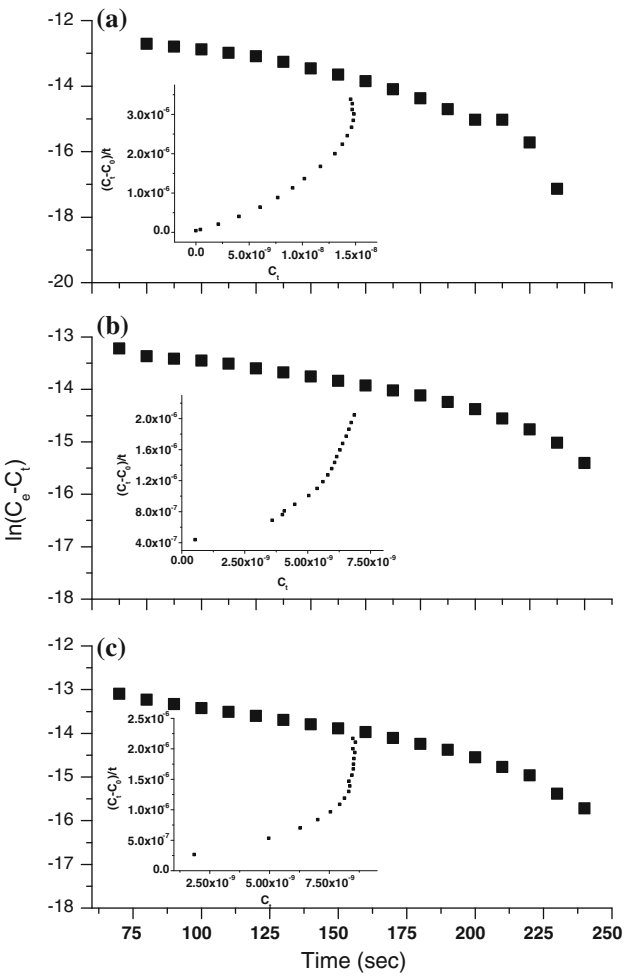

Fig. 11 Variation of $\ln(C_e - C_t)$ vs. t for CuO films of **a** P2, **b** P7, and **c** P10 samples. *Inset* of the Figures shows the plot C_t vs. $C_t - C_0/t$ for the second-order reaction. The linear nature plot shows the first-order kinetics

300 ppm gas. Comparatively significant response toward 50 ppm ammonia of CuO makes it interesting. Several sensors, which were fabricated and tested under identical conditions, exhibited similar gas response. However, the longer recovery time due to slow rate of desorption is the main drawback. More detailed investigations have to be performed in this regard. In future study, we will go on searching the materials added to CuO to improve the sensing performance.

Conclusions

In summary, a simple and economical technique has been used to synthesize nanocrystalline CuO powder. It has been shown that the structural properties of CuO powder can be controlled by pH value in the reaction mixture. The thermal decomposition at pH 10 results in the production of highly active as well as porous nanoparticles of 27 nm in size. A

Table 2 Shows the list of metal oxide film based ammonia sensors. (RT, room temperature)

Sr. No.	Gas sensor material	Response (ppm, sensor operating temperature)	References
1	CuO thick film	1.01 (–, 200 °C)	[51]
2	CuO nanowires	0.06 (1% of air, RT)	[52]
3	$NiFe_2O_4$ thick film	68 (1000, RT)	[53]
4	ZnO thick film	13.69 (300, RT)	[54]
5	Fe_2O_3-activated Cr_2O_3 thick film	9.42 (10, 250 °C)	[55]
6	SnO_2	26 (300, RT)	[56]
7	$LaCo_{0.8}Fe_{0.2}O_3$ thick film	0.97 (300, 200 °C)	[57]

systematic investigation of acidity on the morphology shows that sol–gel auto-combustion technique have a considerable potential for producing CuO nanocrystalline powder having high surface area, maximum porosity, and catalytic activity. The resultant CuO powder in the form of thick film shows high sensitivity for ammonia gas at room temperature, obeys the Elovich equation. First-order reaction kinetics with highest sensor response rate constant in case of CuO nanoparticles when obtained at pH 10 of the precursor solution.

Acknowledgements The authors would like to thank the University Grant Commission for the financial support to carry out the Minor Research Project. The authors also thank Director Indian Institute of Technology Roorkee and Central Instrumentation Laboratory, Panjab University, Chandigarh for providing FESEM, EDAX, and XRD facilities. We gratefully acknowledge instrumentation facility provided by Gurpreet Singh (Samrala) to carry out the electrical characterization.

References

1. Shek CH, Lai JKL, Gu TS, Lin GM (1997) Nanostruct Mater 8(5):605
2. Zhou K, Wang R, Xu B, Li Y (2006) Nanotechnology 17:3939
3. Hu Y, Zhou X, Han Q, Cao Q, Huang Y (2003) Mater Sci Eng B 99:41
4. Sukhorukov YP, Gizhevskii BA, Mostovshchikova EV, Yermakov Ye A, Tugushev SN, Kozlov EA (2006) Tech Phys Lett 32:132
5. Zhu YW, Yu T, Cheong FC, Xu XJ, Lim CT, Tan VBC, Thong JTL, Sow CH (2005) Nanotechnology 16:88
6. Haung LS, Yang SG, Li T, Gu BX, Du YW, Lu YN, Shi SZ (2004) J Cryst Growth 260:130
7. Guan H, Shao C, Chen B, Gong J, Yang X (2003) Inorg Chem Commun 6:1409
8. Li D, Leung YH, Djurisic AB, Liu ZT, Xie MH, Gao J, Chan WK (2005) J Cryst Growth 282:105
9. Wijesundera RP, Hidaka M, Koga K, Sakai K, Siripda W (2006) Thin Solid Films 500:241
10. Lee SY, Mettlach N, Nguyen N, Sun YM, White JM (2003) Appl Surf Sci 206:102
11. Fernandez AI, Calleja A, Chimenos JM, Fernandez MA, Capdevila XG, Serarra M, Xuriguera H, Espiell F (2005) J Sol–Gel Sci Technol 36:11
12. Morales J, Sanchez L, Martin F, Ramos-Barrado JR, Sanchenz M (2004) Electrochim Acta 49:4589
13. Kosugi T, Kaneku S (1998) J Am Ceram Soc 81:3117
14. Papadimitropoulos G, Vourdas N, Vamvaskas VE, Dava Zoglov D (2006) Thin Solid Films 515:2428
15. Zhang Y, Wang S, Qian Y, Zhang Z (2006) Solid State Sci 8:462
16. Pathak LC, Singh TB, Das S, VermaA K, Ramachandrarao P (2002) Mater Lett 57(2):380
17. Zhou J, Wang Y, Zhao F, Wang Y, Zhang Y, Yang L (2006) J Lumin 119:248
18. Hasab MG, Ebrahimi SAS, Badiei A (2007) J Eur Ceram Soc 27:3637
19. Hiremath VA, Venkataraman A (2003) Bull Mater Sci 26:391
20. Kikkawa S (2005) J Am Ceram Soc 88(2):308
21. Lagashetty A, Venkataraman A (2004) Bull Mater Sci 27:491
22. Peng T, Yang H, Pu X, Hu B, Jiang Z, Yan C (2004) Mater Lett 58(3–4):352
23. Purohit RD, Saha S, Tyagi AK (2006) Ceram Int 32(2):143
24. Roya SC, Sharmaa GL, Bhatnagara MC, Manchandab R, Balakrishnanb VR, Samanta SB (2004) Appl Surf Sci 236:306
25. Wu KH, Yu CH, Chang YC, Horng DN (2004) Solid State Chem 177:4119
26. Vajargah SH, Madaah Hosseini HR, Nemati ZA (2006) Mater Sci Eng B 129:211
27. Yue Z, Li L, Zhou J, Zhang H, Gui Z (1999) Mater Sci Eng B 64:68
28. Bedi RK, Singh I (2009) Curr Nanosci 5(3):273
29. Huang J, Zhuang H, Li W (2003) Mater Res Bull 38:149
30. Klug HP, Alexander LE (1974) X-ray diffraction procedure for polycrystalline and amorphous materials, 2nd edn. Wiley, New York, p 687
31. Serin N, Serin T, Horzum S, Celik Y (2005) Semicond Sci Technol 20:398
32. Xu G, Ma H, Zhong M, Zhou J, Yue Y, He Z (2006) J Magn Magn Mater 301:383
33. Williamson GK, Hall WH (1953) Acta Mater 1:22
34. Ramgir NS, Hwang YK, Mulla IS, Chang J (2006) Solid State Sci 8:359
35. Kovacheva D, Godjov H, Petrov K, Mandal S, Lazarraga MG, Pascural L, Amarilla JM, Rojas RM, Herrero P, Rojo JM (2002) J Mater Chem 12:1184
36. Marjan M, Klementina Z, Jadran M (2002) J Power Sources 106:178
37. Riahi-Nooria N, Sarraf-Mamooryb R, Alizadehb P, Mehdikhani A (2008) J Ceram Process Res 9(3):246
38. Park CO, Akbar SA (2003) J Mater Sci 38:4611. doi:10.1023/A:1027402430153
39. Hakim A, Hossain J, Khan KA (2009) Renew Energy 34:2625
40. Devan RS, Kolekar YD, Chougule BK (2006) J Phys Condens Mater 18:9809

41. Bouderbala M, Hamzaoui S, Adnane M, Sahraoui T, Zerdali M (2009) Thin Solid Film 517(5):1572
42. Perez-Ramos ME, Manzano-Ramirez A, Vorobiev PY, Horiey PP, Vorobiev YV, Gonzalez-Hernandez J (2003) Inorg Mater 39:37
43. Jimenez I, Centeno MA, Scotti R, Morazzoni F, Arbiol J, Cornet A, Morante JR (2004) J Mater Chem 14:2412
44. Bedi RK, Singh I (2010) Appl Mater Interfaces 2(5):1361
45. Tongpool R, Yoriya S (2005) Thin Solid Films 477:148
46. Juang RS, Chen ML (1997) Ind Eng Chem Res 36:813
47. Zeldowitsch J (1934) Acta Physicochim URS 1:364
48. Chien SH, Clayton WR (1980) Soil Sci Soc Am J 44:265
49. Richard IM (1996) Principles of adsorption and reaction on solid surfaces. Wiley-Interscience, New York, p 519
50. Khun Khun K, Mahajan A, Bedi RK (2010) Chem Phys Lett 492:119
51. Alexey AT, Gregory PH, Brent TM, John WA (2003) Sens Actuators B 93:126
52. Bejamin JH, Nikolai K, Ganhua L, I-Kuan L, Junhong C, Zin Z (2010) J Phys Chem C 114:2440
53. Kamble RB, Mathe VL (2008) Sens Actuators B 131:205
54. Patil DR, Patil LA, Patil PP (2007) Sens Actuators B 126:368
55. Suryawanshi DN, Patil DR, Patil LA (2008) Sens Actuators B 134:579
56. Deshpande NG, Gudage YG, Sharma R, Vyas JC, Kim JB, Lee YP (2009) Sens Actuators B 138:76
57. Chaudhari GN, Jagtap SV, Gedam NN, Pawar MJ, Sangawar VS (2009) Talanta 78:1136